RSC Advances

PAPER

View Article Online
View Journal | View Issue

Cite this: *RSC Adv.*, 2021, **11**, 23960

Indolylbenzothiadiazoles as highly tunable fluorophores for imaging lipid droplet accumulation in astrocytes and glioblastoma cells†

Kilian Colas,[a] Karl O. Holmberg,[b] Linus Chiang,[c] Susanne Doloczki,[a] Fredrik J. Swartling[b] and Christine Dyrager*[a]

Received 7th June 2021
Accepted 21st June 2021

DOI: 10.1039/d1ra04419b

rsc.li/rsc-advances

We present an extensive photophysical study of a series of fluorescent indolylbenzothiadiazole derivatives and their ability to specifically image lipid droplets in astrocytes and glioblastoma cells. All compounds in the series displayed positive solvatochromism together with large Stokes shifts, and π-extended derivatives exhibited elevated brightness. It was shown that the fluorescence properties were highly tunable by varying the electronic character or size of the *N*-substituent on the indole motif. Three compounds proved capable as probes for detecting small quantities of lipid deposits in healthy and cancerous brain cells. In addition, all twelve compounds in the series were predicted to cross the blood–brain barrier, which raises the prospect for future *in vivo* studies for exploring the role of lipid droplets in the central nervous system.

Introduction

Lipid droplets (LDs) are ubiquitous cellular organelles that serve as reservoirs for natural lipids, such as triglycerides and cholesterol esters.[1] They tend to be excessively abundant in cancer cells, which can use them to reduce excess lipid toxicity, or mobilize them as energy sources to survive tumor starvation.[2–7] Excessive LD accumulation has been recognized as a cancer hallmark,[3,5] and specific imaging of LDs using fluorescent probes has become highly attractive for studying altered lipogenesis in cancer cell biology.[8] Dysregulated LD accumulation (excessive or insufficient) has also been linked to various neurodegenerative disorders,[9,10] including Alzheimer's,[11] Huntingon's[12] and Parkinson's[13] diseases, as well as amyotrophic lateral sclerosis (ALS).[14] While their presence has been observed or suggested in most brain cells,[9] the mechanisms behind their formation and mobilization remain unclear and the available data on LDs in healthy *vs.* cancerous brain tissue is still somewhat contradictory.[2,4,6,7,15] Hence, there is a growing demand for bright and LD-specific fluorophores that are useful for staining LDs in glial cells and brain cancer, such as probes that can detect and monitor small quantities of LDs for studying lipid dynamics in the central nervous system (CNS).[8,16–19]

Herein we report the synthesis, photophysical characterization and cell imaging properties of a series of indolylbenzothiadiazole (InBTD) derivatives. Several of these compounds stained LDs with excellent signal-to-background ratios in both cancerous and healthy brain cells (glioblastoma and astrocytes). The photophysical characteristics of the compounds were extensively studied and correlated to structural diversity, electronical effects and to torsion angle variations between the BTD unit and the indole motif. All compounds in the series were predicted to cross the blood–brain barrier (BBB), which raises the prospect of studies in higher organisms.

Results and discussion

The 2,1,3-benzothiadiazole (BTD) motif has gained popularity as an electron-deficient acceptor unit in donor–acceptor (D–A) fluorophores – compounds that can be used in materials science and/or bioimaging. In general, BTD-based fluorophores exhibit several advantageous features, such as non-toxicity, pronounced solvatochromism, redshifted emission profiles and large Stokes shifts.[20] The latter two are especially relevant for bioimaging since they reduce the risk of background noise that originate from autofluorescence or backscattering from the excitation source.[21]

In this study, we anticipated that an electron-rich indole unit could be an attractive donor counterpart to the BTD core.[20,22] Especially for CNS related bioimaging as it is found in numerous bioactive compounds such as the amino acid tryptophan, the neurotransmitter serotonin, and in various

[a]*Department of Chemistry – BMC, Uppsala University, Box 576, 75123 Uppsala, Sweden. E-mail: christine.dyrager@kemi.uu.se*

[b]*Department of Immunology, Genetics and Pathology, Science for Life Laboratory, Uppsala University, 75185 Uppsala, Sweden*

[c]*Department of Chemistry, University of the Fraser Valley, V2S7M8, Abbotsford, BC, Canada*

† Electronic supplementary information (ESI) available. See DOI: 10.1039/d1ra04419b

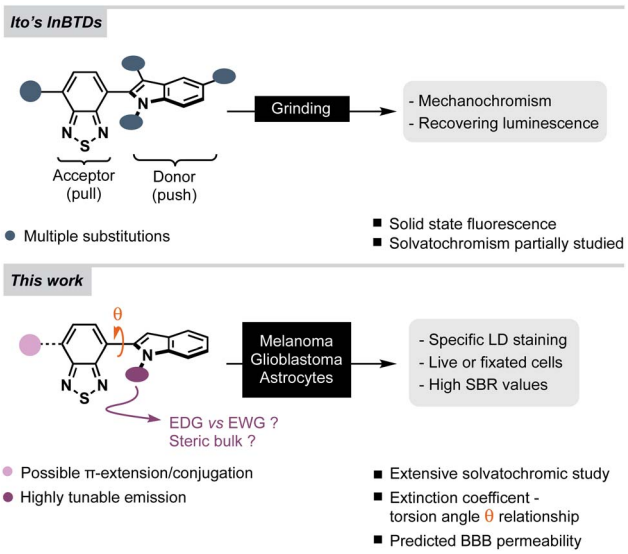

Fig. 1 (Top) Previous studies of the mechanochromic properties of indolylbenzothiadiazoles, InBTDs.[25,26] (Bottom) This work: extensive photophysical characterization in multiple solvents and intracellular lipid droplet (LD) staining in melanoma, glioblastoma and astrocytes. SBR = signal-to-background ratio.

psychotropic drugs – all of which have BBB permeability.[23,24] InBTDs have so far mainly been reported by the Ito group for their interesting mechanochromic properties (Fig. 1, top).[25,26] Thus, in this work we wanted to explore their utility as imaging agents for fluorescent cell microscopy and also study how different *N*-substituents on the indole motif affect the photophysical properties (Fig. 1, bottom). We hypothesized that the size of the *N*-substituent would regulate the fluorescence efficiency through the BTD–indole torsion angle (θ), while the electronic nature, electron-donating groups (EDGs) or electron-withdrawing groups (EWGs), would impact the D–A character of the fluorophores. Accordingly, we synthesized twelve InBTDs (**1–12**, Scheme 1A) with such features, of which four included an additional aromatic motif to extend the π-conjugation and thereby obtain increased molar absorptivity.

DFT calculations

Geometry optimization of InBTDs **1–12** (Scheme 1A) were performed without symmetry constraints using the hybrid M06 functional and 6-31g* basis set combination,[27–29] and the corresponding polarized continuum model (PCM)[30] for the corresponding solvents (hexane, toluene, THF, DMSO, acetonitrile, isopropanol, MeOH and H_2O). For full computational details, see ESI pp. 27–34.† This combination of functional and basis set has previously been used to investigate the electronic structures of similar BTD-containing compounds.[31] All compounds in the series (**1–12**) exhibited a calculated BTD-to-indole bond distance of *ca.* 1.46 Å. Compounds **1** and **9** exhibited no or negligible twisting ($\theta = 0.0$ and <1.0°, respectively) between the aromatic BTD and the unprotected indole ring due to

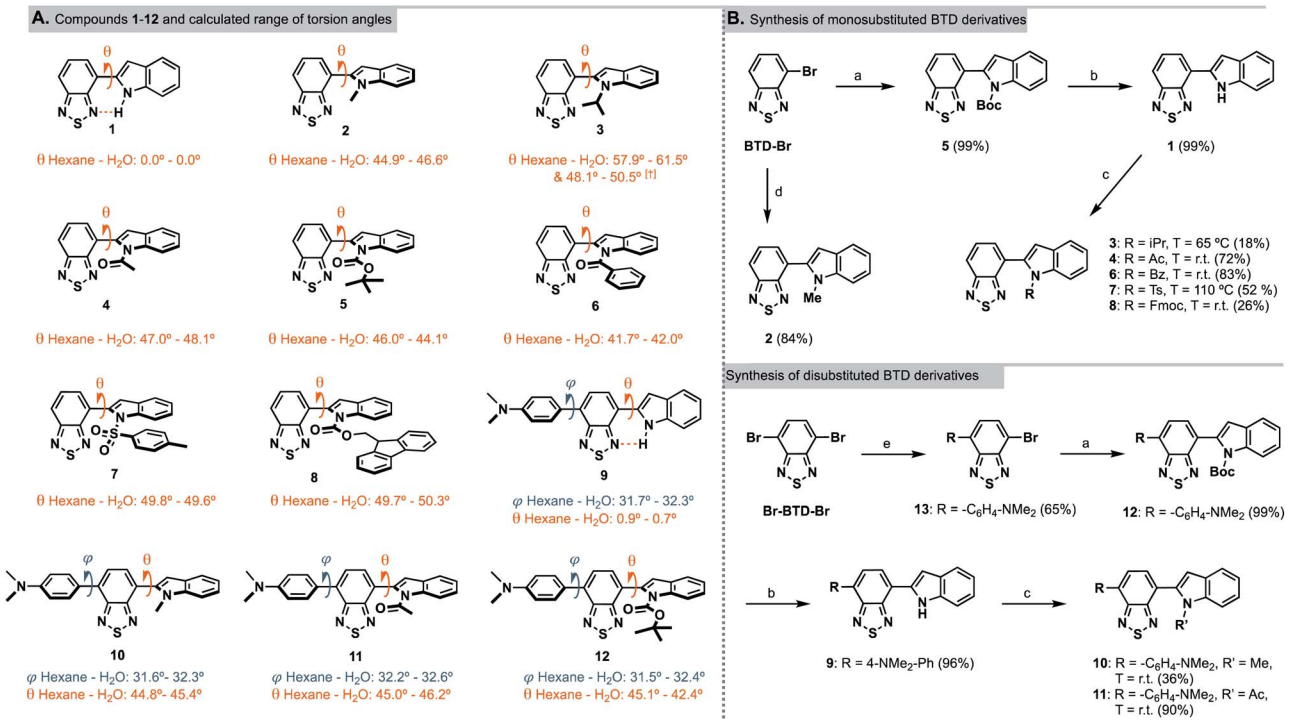

Scheme 1 (A) Chemical structures of InBTDs **1–12** and their calculated torsion angles in hexane and water (least to most polar solvent investigated).† Two stable conformers found. (B) Synthetic routes for the monosubstituted (top) and the disubstituted BTD derivatives (bottom). Reagents and conditions: (a) *N*-Boc-indole-2-boronic acid, PEPPSI-Ipr, K_2CO_3, toluene/MeOH (1 : 1), 80 °C, 2 h; (b) trifluoroacetic acid, DCM, 0 °C to r.t., 16 h; (c) R–Cl or R–Br, NaH, 15-crown-5, DMF, 0 °C to indicated *T*, 16 h; (d) 1-methyl-2-indoleboronic acid pinacol ester, PEPPSI-Ipr, K_2CO_3, toluene/MeOH (1 : 1), 80 °C, 2 h; (e) 4-(*N*,*N*-dimethylamino)phenylboronic acid pinacol ester, $Pd(PPh_3)_4$, Na_2CO_3 (2 M aq.), toluene/EtOH (1 : 10), 85 °C, 16 h.

intramolecular hydrogen bonding between the H-*N*-indole and the BTD fragment (further discussed below). All other compounds (**2–8**, **10–12**) displayed torsion angles (θ) greater than 40°, which can be attributed to the absence of hydrogen bonding and increased steric bulk of the *N*-substituent. Compounds **9–12** also showed twisting between the 4-(*N*,*N*-dimethylamino)phenyl and the BTD unit (φ) of *ca.* 30°. Vertical excitation energies were calculated using time-dependent density functional theory (TD-DFT) at the same level of theory with the corresponding PCM. In all cases, vertical excitations originated from HOMO → LUMO transitions, where the HOMO was delocalized over the entire molecule, and the LUMO was predominantly BTD-based (ESI Fig. S18†). The disubstituted compounds (**9–12**) were predicted to exhibit red-shifted transitions in comparison to their monosubstituted counterparts (**1**, **2**, **4** and **5**). Furthermore, compounds **1–8** were predicted to exhibit blue-shifted absorptions in more polar solvents, while a far less pronounced trend was predicted for the compounds containing the 4-(*N*,*N*-dimethylamino)phenyl substituent (**9–12**). These predicted trends were proven to be in good agreement with experimental UV-Vis spectra collected in the corresponding solvents (*vide infra*).

Synthesis

Following literature precedents,[25,32] compounds **2** and **5** were prepared in excellent yields (84 and 99%, respectively) using a Suzuki–Miyaura cross-coupling protocol. Accordingly, 4-bromo-2,1,3-benzothiadiazole (**BTD-Br**) and the appropriate indolyl-boronic acid were coupled using PEPPSI-Ipr as the

Table 1 Photophysical data of the BTD derivatives **1–12** in solvents of different polarity

Solvent	Comp.	λ_{Amax} [nm]	λ_{Emax} [nm]	Stokes shift[a] [nm]	ε [M^{-1} cm^{-1}]	Φ_F	Comp.	λ_{Amax} [nm]	λ_{Emax} [nm]	Stokes shift [nm]	ε [M^{-1} cm^{-1}]	Φ_F
Hexane		452	509	57	6600	0.02		368	480	112	7900	0.17
Toluene		448	542	94	8400	0.06		368	495	127	4700	0.60
THF	**1**	434	565	131	8000	0.17	**7**	358	503	145	5000	0.50
DMSO		429	608	179	6700	0.02		354	524	170	8100	0.55
MeCN		424	601	177	6800	0.02		350	517	167	5700	0.55
i-PrOH		436	600	164	8000	0.07		358	529	171	5300	0.19
Hexane		415	517	102	5500	0.86		368	492	124	5100	0.69
Toluene		415	555	140	4300	0.36		370	516	146	3800	0.63
THF	**2**	408	575	167	4700	0.16	**8**	365	523	158	4700	0.57
DMSO		404	623	219	4700	0.01		367	554	187	3600	0.15
MeCN		395	609	214	4600	0.01		361	546	185	3800	0.41
i-PrOH		408	n.e.[b]	—	5100	—		364	552	188	4300	0.09
Hexane		414	518	104	2500	0.63		494	568	74	n.d.[c]	0.57
Toluene		411	555	144	300	0.20		491	604	113	2200	0.21
THF	**3**	401	478	177	1200	0.10	**9**	495	649	154	21 400	0.11
DMSO		396	n.e.[b]	—	400	—		478	558	80	2700	0.02
MeCN		385	n.e.[b]	—	1200	—		487	697	210	17 000	0.01
i-PrOH		402	n.e.[b]	—	400	—		490	661	171	8300	<0.01
Hexane		382	499	117	5400	0.18		460	564	104	n.d.[c]	0.75
Toluene		381	520	139	5200	0.22		464	604	140	1300	0.40
THF	**4**	376	537	161	6000	0.15	**10**	463	638	175	6200	0.20
DMSO		373	571	198	3900	0.07		464	668	204	1400	<0.01
MeCN		367	563	196	3000	0.07		452	680	228	6600	0.02
i-PrOH		373	569	196	5500	0.01		461	631	170	1400	<0.01
Hexane		371	488	117	4500	0.79		452	560	108	n.d.[c]	0.89
Toluene		373	510	137	6300	0.88		464	612	148	13 700	0.43
THF	**5**	369	521	152	5000	0.68	**11**	462	648	186	13 700	0.15
DMSO		367	553	186	5000	0.48		464	562	98	13 100	0.02
MeCN		363	548	185	5100	0.46		452	694	242	9800	0.02
i-PrOH		368	557	189	5700	0.07		460	608	148	n.d.[c]	0.01
Hexane		384	495	111	8200	0.23		441	551	110	n.d.[c]	0.85
Toluene		385	518	133	5900	0.24		452	599	147	11 100	0.56
THF	**6**	381	531	150	5200	0.16	**12**	452	635	183	13 000	0.22
DMSO		377	563	186	5600	0.11		458	562	104	13 200	0.02
MeCN		372	555	183	6400	0.10		445	693	248	12 000	0.02
i-PrOH		378	562	184	2900	0.02		449	632	183	n.d.[c]	0.01

[a] Stokes shift in nm = $\lambda_{Emax} - \lambda_{Amax}$. [b] No emission detected. [c] Not determined due to poor solubility.

catalyst (Scheme 1B, top). To introduce other *N*-substituents on the indole – when the boronic acids were not commercially available – we found it more straightforward to proceed *via* *N*-functionalization of the unsubstituted indole motif. Hence, the Boc group in compound **5** was removed with trifluoroacetic acid to quantitatively provide the *N*-H derivative **1**. Subsequently, **1** was deprotonated with sodium hydride and treated with various alkyl, acyl and sulfonyl chlorides, which initially resulted in very low yields. Noting the intense purple color of the reaction mixture upon deprotonation, we hypothesized that the conjugate base of **1** may strongly chelate to the sodium cation from the hydride base and hinder reactivity towards the electrophiles. Consequently, one equivalent of 15-crown-5 was added to abstract the sodium counterion, resulting in improved yields.

The *N*-acetyl and *N*-benzoyl derivatives **4** and **6** were obtained in high yields (72 and 83%, respectively) at room temperature, while tosylation required heating at 110 °C to provide **7** in 52% yield (observed in NMR as a mixture of rotamers). InBTDs with bulkier substituents remained challenging to synthesize. Nonetheless, the isopropyl derivative **3** could be obtained in 18% yield upon heating to 65 °C (the boiling point of the electrophile). On the other hand, heating proved detrimental to the preparation of the Fmoc-protected **8**, which was obtained in 26% yield at room temperature. Unlike previously reported InBTD derivatives,[25,26] the compounds in this series were left unfunctionalized on the C-3 position of the indole. As a consequence, competing C-3 reactivity was observed when attempting other synthetic strategies. In particular, transition-metal catalyzed C–N coupling reactions led to dimerization of **1** at the C-3 position, presumably due to a strong directing group effect of the BTD core. Likewise, the use of anhydrides as electrophiles mostly resulted in C-3 acylation.

To improve the molar absorptivities of the compounds,[33] we introduced an additional aromatic substituent at the 4-position of the BTD core starting from 4,7-dibromo-2,1,3-benzothiadiazole, **Br-BTD-Br** (Scheme 1B, bottom). First, Suzuki–Miyaura coupling conditions were used to prepare the 4-(*N*,*N*-dimethylamino)phenyl substituted bromo-BTD intermediate **13** in 65% yield. A second coupling afforded the Boc-protected InBTD derivative **12**, followed by deprotection to yield **9** in quantitative yields. The addition of 15-crown-5 was again crucial to prepare both the methyl- and acetyl-functionalized compounds **10** and **11** in 36% and 90% yield, respectively.

Photophysical characterization

The photophysical properties of compounds **1–12** were investigated by UV-absorption and fluorescence spectroscopy in a broad variety of solvents of different polarity (Table 1 and ESI Fig. S1–S12†). Due to solubility issues, isopropanol was used instead of methanol, and measurements in water were excluded since the analysis could not be performed reliably. Several photophysical trends and behaviors could be noticed when changing the nature of the indole *N*-substituent. For the monosubstituted compounds **2–8**, a clear correlation was observed between the molar extinction coefficients (ε) and the calculated torsion angles, which is best represented in hexane where the smallest solvent effects are expected (Fig. 2, top). As θ increases, the conjugation of the D–A system is weakened and ε decreases. Accordingly, the isopropyl derivative **3** ($\theta = 57.9°$) showed the lowest ε value (2500 M^{-1} cm^{-1}) and the benzoyl derivative **6** ($\theta = 41.7$) the highest (8200 M^{-1} cm^{-1}). The tosyl-derivative **7** displayed a clear exception to this trend ($\theta = 49.8°$, $\varepsilon = 7900$ M^{-1} cm^{-1}), likely due to conjugation of the sulfonyl group to the aromatic π-system. Also, the unprotected *N*-H compound **1**, which calculations suggest should be flat ($\theta = 0°$), showed similar ε values as for many of the other derivatives and no increased values caused by planarization. The disubstituted compounds **9–12**, which are larger conjugated systems, displayed up to three times higher ε values than the monosubstituted analogues. Moreover, while the ε values differ between the derivatives in the series, they were rather uniform regardless of solvent for each compound.

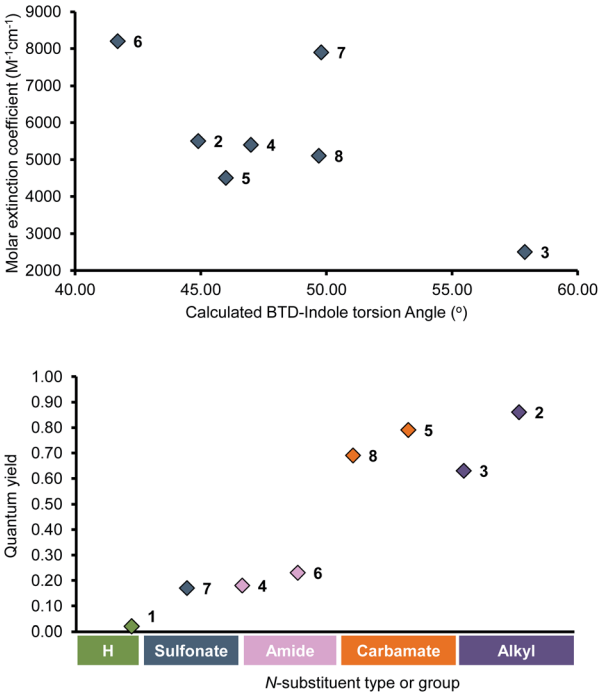

Fig. 2 (top) Correlation between molar extinction coefficients (ε) and calculated torsion angles (θ) in hexane for InBTDs **2–8**; (bottom) representation of the relationship between quantum yield Φ and the nature of the indole *N*-substituent in hexane for InBTDs **1–8**.

However, a few exceptions were observed for **3**, **9** and **10** where ε varied dramatically in different solvents (*e.g.*, **9**, $\varepsilon =$ 2200 M^{-1} cm^{-1} in toluene *vs.* 21 400 in THF). Further comparing the monosubstituted derivatives **1–8** in hexane revealed that the fluorescence quantum yield Φ_F was highly affected by the electronic character of the indole *N*-substituent (Fig. 2, bottom). Compounds **2** and **3** with EDGs (alkyls, methyl or isopropyl) showed excellent quantum yields ($\Phi_F = 0.85$ and 0.63) while **4**, **6** and **7** with EWGs (amide or sulfonate) gave much lower values ($\Phi_F = 0.18$, 0.23 and 0.17). As an exception, the carbamate derivatives **5** and **8** showed very high fluorescence efficiency ($\Phi_F = 0.79$ and 0.69), despite the EWG character

of the *N*-protecting group. The unprotected *N*-H derivative **1** displayed low fluorescent quantum yields in all solvents (Φ_F = 0.02–0.07) except THF ($\Phi_F = 0.17$). As previously reported, this is likely due to strong intramolecular hydrogen-bonding.[25,34–36] Furthermore, the photophysical behavior for the disubstituted analogue **9** differed from **1**, even though the calculated torsion angles θ were close to zero in all solvents (θ = 0.7°–0.9°). Instead, it followed the trends of compounds bearing electron-donating *N*-substituents on the indole motif (*i.e.*, **2**, **3** and **10**). The same trend also applied for the disubstituted derivatives with EWGs on the indole (**11** and **12**), showing that the quantum yields for these were highly affected by the additional donor motif, 4-(*N*,*N*-dimethylamino)phenyl. Compounds **2**, **3** and **9–12** displayed good to excellent quantum yields in hexane, which gradually decreased with increasing solvent polarity becoming largely quenched in DMSO, acetonitrile and isopropanol. For the isopropyl derivative **3**, the quenching was so pronounced that no emission could be detected in these solvents. As these compounds are the strongest D–A (**2**, **3**) or D–A–D (**9**, **10**) systems in the series, this behavior can be ascribed to a stronger stabilization of their excited states in polar environments.[37–43] This is in line with the strong positive solvatochromism observed in all cases,[43] where emission maxima gradually increased with solvent polarity, resulting in large Stokes shifts. On the other hand, the absorption maxima (λ_{Amax}) were generally unaffected by the solvent, although a slight negative solvatochromism was observed, followed by a small uptick in isopropanol. This suggests that solvent stabilization effects are also at play in the ground state.

Other trends were observed for the monosubstituted compounds **4–8** that contain protecting groups with electron-withdrawing character on the indole motif. Their emission and absorption profiles were more blue-shifted and their quantum yields generally decreased with solvent polarity. However, the latter was either less pronounced (*e.g.*, in DMSO and acetonitrile for **5** and **8**) or more irregular (**4**, **6** and **7**). This indicates that the withdrawing nature of the *N*-substituent partially negates the donation character of the indole group in the push–pull system. Nevertheless, they still displayed strong positive solvatochromism and remarkably large Stokes shifts (*e.g.*, 189 nm for **5** in isopropanol). We could also observe that the carbamate derivatives **5** and **8** had high or excellent quantum yields in most of the solvents. They even displayed high values in acetonitrile ($\Phi_F = 0.46$ and 0.41, respectively).

Lippert–Mataga (L–M) plots of all compounds (ESI Fig. S13 and S14†) further support solvatochromism as the main cause for the observed spectral shifts, as the correlation between Stokes shifts and solvent polarizability are linear.[44,45] However, for the disubstituted compounds **9–12**, some aberrations could be seen. First, a clear deviation from the linear trend of **9** in DMSO stems from hydrogen bonding between the solvent and the unprotected indole.[35,36] The reason why this was observed for **9**, and not for the monosubstituted analogue **1**, presumably arise from the presence of a weaker intramolecular hydrogen bond ($\theta \neq 0°$, Scheme 1A) – caused by the presence of the additional donor substituent, 4-(*N*,*N*-dimethylamino)phenyl. Measurements of compounds **10–12** in isopropanol also deviated from the linear trend in the L–M plots. This was again likely due to hydrogen bonding, but this time between the protic solvent and the 4-(*N*,*N*-dimethylamino)phenyl motif. Furthermore, the emission profiles of **11** and **12** in DMSO displayed a very pronounced dual emission (ESI Fig. S11 and S12†). This a is a well-known phenomenon in D–A fluorophores that can be ascribed to a locally excited (LE) state and an intramolecular charge transfer (ICT) state – the latter being stabilized by polar solvents.[37,46,47] The involvement of ICT states are typically associated with solvatochromism and decreased quantum yields with increasing solvent polarity,[37,39] which is consistent with our observations. Moreover, the absorption spectra of **1–3** displayed distinct shoulders in hexane, and to a lesser extent in toluene and THF. This suggests the presence of two ground-state species that can be attributed to two different stable conformations. In the case of **1**, with or without intramolecular hydrogen bonding and in the case of **3**, the presence of steric bulk (isopropyl group) that generates rotamers. The latter is supported by our calculations (ESI p. 31†), which show two stable conformational isomers, one of which display the largest torsion angles in the series (θ = 57.9–61.5°) between the indole motif and the BTD unit. While the calculations do not indicate the same for compound **2**, a similar effect may occur that is not reflected by the DFT model. In all three cases (**1–3**), a single emission band was observed, suggesting the existence of a single excited state. Thus, rapid rotamer interconversion in the excited state is less likely, as it would violate the non-equilibration of excited rotamers (NEER) principle.[48] Although, such behavior has been reported in recent literature for D–A fluorophores.[49,50] In a more subtle case, **7** showed slight shoulders in both the absorption and emission spectra, suggesting that two ground-state rotamers (which were observed in NMR) are converted to two distinct excited-state rotamers that do follow the NEER principle.

Cell studies

Several BTD-based fluorophores have shown to specifically stain LDs in cancer cells, including our recently reported dyes.[32,51] We therefore wanted to explore the utility of InBTDs **1–12** as imaging agents for fluorescent cell microscopy. Three different cell lines were chosen for the study: malignant melanoma cells (SK-MEL-28), which contain a significant number of LDs.[52] Glioblastoma cells (U1242MG) and normal human astrocytes (NHA) were also investigated, given the surge of interest of LDs in brain cancer,[2,4,6,7] LDs role in neurodegenerative diseases[9,11–14] as well as the prevalence of the indole motif in BBB-crossing substances.[23,24] Live cells were incubated with compounds **1–12** (10 μM) for 24 h and subsequently fixated and costained with DAPI prior to fluorescence microscope imaging. The results showed that the InBTD derivatives **5**, **9**, **11** and **12**, which exhibit the most pronounced brightness in apolar solvents ($\varepsilon \times \Phi_F \geq 4000\ M^{-1}\ cm^{-1}$ in hexane and toluene), were supreme in the series for obtaining clear and favorable signals in cells (Fig. 3 and ESI Fig. S15, S16†). For instance, the monosubstituted compound **5** gave a characteristic LD pattern in melanoma cells (ESI Fig. S15†) with a good signal-to-

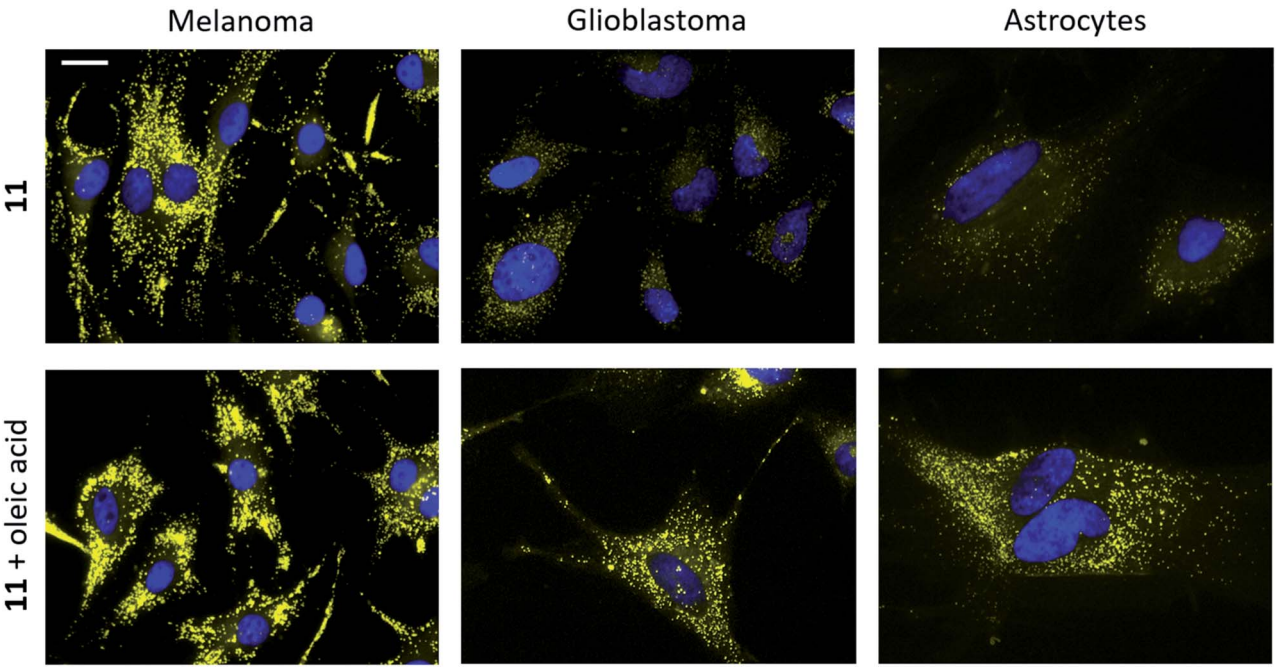

Fig. 3 Staining of melanoma (SK-MEL-28, left), glioblastoma (U1242MG, middle) and normal human astrocytes (NHA, right) with **11** (10 μM, top and bottom) and oleic acid supplementation (100 μM, bottom). Staining was performed on live cells, which were fixated after 24 h incubation. Cell nuclei were stained with DAPI (seen in blue).[54] Scale bar: 20 μm.

background ratio (SBR = 1.9) in the green channel.[53] However, the signal contrast was much less favorable for **5** in glioblastoma cells and astrocytes (SBR = 1.8 and 1.7, respectively). This observation was likely attributed to (i) the lower amount and smaller size of LDs in these cells lines compared to melanoma cells and (ii) the modest brightness of **5** (*e.g.*, 5544 M^{-1} cm^{-1} in toluene), which evidently is not optimal for detecting low quantities of LDs. Nevertheless, the brighter disubstituted compounds, **11** (Fig. 3, top) and **12** (ESI Fig. S15†), gave excellent results in all three cell lines, providing a clear LD staining pattern in the yellow channel[53] with excellent signal distinction (for **11**, SBR = 14.0, 5.0, and 5.6 in melanoma, glioblastoma and astrocytes, respectively). They also showed no or very low signal in the blue, green and red channels[53] (ESI Fig. S17†), making them highly suitable for multicolor imaging with different fluorophores. Furthermore, compound **9** gave an unexpected worm-shaped pattern in the yellow and red channels[53] (ESI Fig. S16†) when using our standard staining protocol (*i.e.*, post-fixation after live cell treatment). Notably, the same pattern was observed in live-cell imaging experiments. While this could be due to precipitation in the cell medium, the shape of the putative aggregates seems to rule out crystallization. Instead, we propose that the unprotected indole moiety (made more nucleophilic by the electron donating 4-(*N*,*N*-dimethylamino) phenyl substituent) reacts with components of the cell culture medium. Nonetheless, **9** proved to be an excellent stain for fixed cells, providing a bright signal in the yellow channel,[54] after 30 min treatment, with an LD-staining pattern comparable to the other probes (ESI Fig. S16†). All our cell imaging experiments with **5**, **9**, **11** and **12** resulted in punctate patterns that are consistent with intracellular LD staining from the literature.[8,17,32]

To further verify LD staining, co-staining with standard fluorescent LD markers (*e.g.*, Nile Red) could not be performed due to overlapping photophysical profiles. Instead, co-staining of compound **11** was performed using immunofluorescence with an antibody for adipophilin – a protein that is localized on the surface of LDs.[17] The results clearly showed colocalization of **11** and adipophilin, which confirms LD staining (ESI Fig. S18†). Cells were also supplemented with oleic acid, a process known to strongly enhance LD formation.[2,17] As depicted in Fig. 3, cell staining experiments were performed with **11** in the absence and presence of oleic acid (top and bottom panels, respectively). The latter showed a significant increase in both signal intensity and in the number of droplet-like items in all three cell lines, strongly supporting LD specific staining. The fluorescent cell images also revealed significant differences between the different cell lines. While LDs were more abundant and visibly larger in melanoma than in glioblastoma cells, they appeared to be distributed around the entire cell in a uniform fashion. In contrast, the healthy NHA exhibited much fewer LDs that seemed to be located in the periphery of the cells rather than close to the nucleus. The results clearly showed detectable LDs in NHAs, in accordance with the most recent literature.[6,7,15,54] The observed differences between the cell lines were also consistent with mounting evidence that cancer cells rely on modified lipid metabolism and increased quantities of LDs to promote tumor survival by resisting cell starvation and lipid toxicity.[3,5]

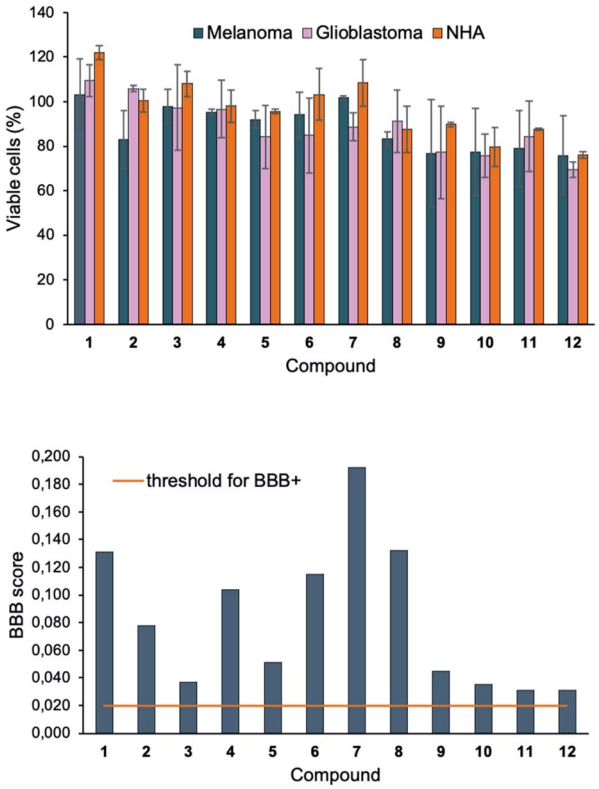

Fig. 4 (Top) Cell viability of melanoma (SK-MEL-28, blue), glioblastoma (U1242MG, pink) and normal human astrocytes (NHA, orange) after treatment with **1–12** (10 μM) for 24 h, measured by resazurin staining assay. Results are represented as % of a DMSO control as a mean ± standard deviation of results obtained from triplicates and twice repeated independent experiments. (Bottom) Graphical representation of BBB^+ scores for **1–12**. The orange horizontal line represents the threshold for predicted positive BBB crossing.

The cell viability after treatment of **1–12** (10 μM) was investigated using the resazurin assay (Fig. 4, top). No significant signs of toxicity could be observed after 24 h incubation. However, the disubstituted compounds **9–12** showed a very modest decrease in viability compared to their monosubstituted counterparts. To explore the future potential of the compounds for *in vivo* CNS imaging, **1–12** were further evaluated using Xie's platform for BBB penetration (see ESI†).[55] The model predicted that all compounds in the series could cross the BBB (Fig. 4, bottom), although with different grades of capacity. For example, the BBB^+ scores for the brighter disubstituted compounds **9–12** were generally lower than for the majority of the monosubstituted derivatives **1–8** – an effect that suggestively originates from increased hydrogen bond ability in the presence of the 4-(*N*,*N*-dimethylamino)phenyl motif.

Conclusions

We have described a series of solvatochromic indolyl–BTD derivatives, whose fluorescence properties can be highly tuned *via* the *N*-substituent on the indole motif – either by varying its electronic nature (EDGs *vs.* EWGs) or steric bulk. The latter which affects the torsion angle between the aromatic units and thus the degree of conjugation within the molecules. Introduction of an electron-donating moiety, 4-(*N*,*N*-dimethylamino) phenyl, at the 4-position of the BTD core gave disubstituted derivatives with improved brightness and red-shifted emission profiles. Among those, compound **9**, **11** and **12** proved to be excellent probes for specific imaging of lipid droplets in melanoma cells, and also for staining lower quantities of lipid accumulation in cancerous and healthy brain cells (glioblastoma and astrocytes).

These compounds are easily synthesized, exhibit large Stokes shifts, allows for multicolor imaging and are predicted to cross the BBB. They also show superior emissive properties in hydrophobic environments and display suppressed emission in polar protic solvents – an ideal trait for staining lipid deposits with high contrast in cells. Notably, they do not suffer from unspecific staining or background artifacts (attributed to small Stokes shifts) – known limitations for commonly used and commercialized LD probes such as Nile Red and BODIPY-based derivatives.[13] Thus, we believe that compound **9**, **11** and **12** will be valuable additions to the available collection of LD-dyes,[8] particularly for imaging LDs in brain tissue that require high specificity and excellent signal-to-background ratios.[2,4,6,7,9,11–14] Also, their predicted BBB permeability raises the future prospects for *in vivo* studies to investigate altered lipogenesis in the CNS.

Conflicts of interest

The authors declare no competing financial interest.

Acknowledgements

This work was supported by the Swedish Research Council, Dnr: 2018-03524 (to CD), the Carl Trygger Foundation, Dnr: CTS 18:90 (to CD) and a NSERC Discovery Grant (to LC). Compute-Canada is acknowledged for access to computational resources. We also thank Prof. Katarina Edwards and her group for access to their spectrofluorometer and Dr Lukasz Pilarski for proofreading the manuscript.

Notes and references

1 J. A. Olzmann and P. Carvalho, *Nat. Rev. Mol. Cell Biol.*, 2019, **20**, 137–155.
2 B. Taïb, A. M. Aboussalah, M. Moniruzzaman, S. Chen, N. J. Haughey, S. F. Kim and R. S. Ahima, *Sci. Rep.*, 2019, **9**, 19593.
3 T. Petan, E. Jarc and M. Jusović, *Molecules*, 2018, **23**, 1941.
4 F. Geng and D. Guo, *Int. Med. Rev.*, 2017, **3**, DOI: 10.18103/imr.v18103i18105.18443.
5 A. L. S. Cruz, E. d. A. Barreto, N. P. B. Fazolini, J. P. B. Viola and P. T. Bozza, *Cell Death Dis.*, 2020, **11**, 105.
6 C. N. Barber and D. M. Raben, *Front. Cell. Neurosci.*, 2019, **13**, 212.
7 B. C. Farmer, J. Kluemper and L. A. Johnson, *Cells*, 2019, **8**, 182.

8 T. K. Fam, A. S. Klymchenko and M. Collot, *Materials*, 2018, **11**, 1768.
9 B. C. Farmer, A. E. Walsh, J. C. Kluemper and L. A. Johnson, *Front. Neurosci.*, 2020, **14**, 742.
10 V. Teixeira, P. Maciel and V. Costa, *Biochim. Biophys. Acta, Mol. Cell Biol. Lipids*, 2021, **1866**, 158820.
11 L. K. Hamilton, M. Dufresne, S. E. Joppé, S. Petryszyn, A. Aumont, F. Calon, F. Barnabé-Heider, A. Furtos, M. Parent, P. Chaurand and K. J. L. Fernandes, *Cell Stem Cell*, 2015, **17**, 397–411.
12 M. Martinez-Vicente, Z. Talloczy, E. Wong, G. Tang, H. Koga, S. Kaushik, R. de Vries, E. Arias, S. Harris, D. Sulzer and A. M. Cuervo, *Nat. Neurosci.*, 2010, **13**, 567–576.
13 S. Fanning, D. Selkoe and U. Dettmer, *npj Parkinson's Dis.*, 2020, **6**, 3.
14 G. Pennetta and M. A. Welte, *Dev. Cell*, 2018, **45**, 427–432.
15 M. S. Ioannou, J. Jackson, S.-H. Sheu, C.-L. Chang, A. V. Weigel, H. Liu, H. A. Pasolli, C. S. Xu, S. Pang, D. Matthies, H. F. Hess, J. Lippincott-Schwartz and Z. Liu, *Cell*, 2019, **177**, 1522–1535.e1514.
16 X. Ren, F. Zhang, H. Luo, L. Liao, X. Song and W. Chen, *Chem. Commun.*, 2020, **56**, 2159–2162.
17 L. L. Listenberger and D. A. Brown, *Curr. Protoc. Cell Biol.*, 2007, **35**, 24.22.21.
18 J. Rumin, H. Bonnefond, B. Saint-Jean, C. Rouxel, A. Sciandra, O. Bernard, J.-P. Cadoret and G. Bougaran, *Biotechnol. Biofuels*, 2015, **8**, 42.
19 A. Loudet and K. Burgess, *Chem. Rev.*, 2007, **107**, 4891–4932.
20 B. A. D. Neto, P. H. P. R. Carvalho and J. R. Correa, *Acc. Chem. Res.*, 2015, **48**, 1560–1569.
21 L. D. Lavis and R. T. Raines, *ACS Chem. Biol.*, 2008, **3**, 142–155.
22 D. Jiang, S. Chen, Z. Xue, Y. Li, H. Liu, W. Yang and Y. Li, *Dyes Pigm.*, 2016, **125**, 100–105.
23 N. K. Kaushik, N. Kaushik, P. Attri, N. Kumar, C. H. Kim, A. K. Verma and E. H. Choi, *Molecules*, 2013, **18**, 6620–6662.
24 Y. Ban, Y. Murakami, Y. Iwasawa, M. Tsuchiya and N. Takano, *Med. Res. Rev.*, 1988, **8**, 231–308.
25 S. Ito, T. Yamada, T. Taguchi, Y. Yamaguchi and M. Asami, *Chem.–Asian J.*, 2016, **11**, 1963–1970.
26 S. Ito, T. Taguchi, T. Yamada, T. Ubukata, Y. Yamaguchi and M. Asami, *RSC Adv.*, 2017, **7**, 16953–16962.
27 G. A. Petersson and M. A. Al-Laham, *J. Chem. Phys.*, 1991, **94**, 6081–6090.
28 M. M. Francl, W. J. Pietro, W. J. Hehre, J. S. Binkley, M. S. Gordon, D. J. DeFrees and J. A. Pople, *J. Chem. Phys.*, 1982, **77**, 3654–3665.
29 P. C. Hariharan and J. A. Pople, *Theor. Chim. Acta*, 1973, **28**, 213–222.
30 M. Cossi, G. Scalmani, N. Rega and V. Barone, *J. Chem. Phys.*, 2002, **117**, 43–54.
31 J. E. Barnsley, G. E. Shillito, C. B. Larsen, H. van der Salm, L. E. Wang, N. T. Lucas and K. C. Gordon, *J. Phys. Chem. A*, 2016, **120**, 1853–1866.
32 H. Appelqvist, K. Stranius, K. Börjesson, K. P. R. Nilsson and C. Dyrager, *Bioconjugate Chem.*, 2017, **28**, 1363–1370.
33 Y. Lee, A. Jo and S. B. Park, *Angew. Chem., Int. Ed.*, 2015, **54**, 15689–15693.
34 C. Shang, G. Wang, K. Liu, Q. Jiang, F. Liu, P.-T. Chou and Y. Fang, *Angew. Chem., Int. Ed.*, 2020, **59**, 8579–8585.
35 G. Wiosna, I. Petkova, M. S. Mudadu, R. P. Thummel and J. Waluk, *Chem. Phys. Lett.*, 2004, **400**, 379–383.
36 J. Waluk, *Acc. Chem. Res.*, 2003, **36**, 832–838.
37 Z. R. Grabowski, K. Rotkiewicz and W. Rettig, *Chem. Rev.*, 2003, **103**, 3899–4032.
38 A. S. Klymchenko, *Acc. Chem. Res.*, 2017, **50**, 366–375.
39 K. Bhattacharyya and M. Chowdhury, *Chem. Rev.*, 1993, **93**, 507–535.
40 G. Haberhauer, *Chem.–Eur. J.*, 2017, **23**, 9288–9296.
41 Z. Zhang, G. Zhang, J. Wang, S. Sun and Z. Zhang, *Comput. Theor. Chem.*, 2016, **1095**, 44–53.
42 C. Zhong, *Phys. Chem. Chem. Phys.*, 2015, **17**, 9248–9257.
43 P. Suppan, *J. Photochem. Photobiol., A*, 1990, **50**, 293–330.
44 N. Mataga, Y. Kaifu and M. Koizumi, *Bull. Chem. Soc. Jpn.*, 1955, **28**, 690–691.
45 L. Ernst, *Z. Phys. Chem.*, 1956, **6**, 125–128.
46 D. Liese and G. Haberhauer, *Isr. J. Chem.*, 2018, **58**, 813–826.
47 S. Sasaki, G. P. C. Drummen and G.-i. Konishi, *J. Mater. Chem. C*, 2016, **4**, 2731–2743.
48 J. K. Whitesell, M. A. Minton and V. D. Tran, *J. Am. Chem. Soc.*, 1989, **111**, 1473–1476.
49 A. Cesaretti, B. Carlotti, F. Elisei, C. G. Fortuna and A. Spalletti, *Phys. Chem. Chem. Phys.*, 2018, **20**, 2851–2864.
50 A. Cesaretti, B. Carlotti, F. Elisei, C. G. Fortuna, G. Consiglio and A. Spalletti, *Phys. Chem. Chem. Phys.*, 2017, **19**, 5262–5272.
51 K. Colas, S. Doloczki, A. Kesidou, L. Sainero-Alcolado, A. Rodriguez-Garcia, M. Arsenian-Henriksson and C. Dyrager, *ChemPhotoChem*, 2021, **5**, DOI: 10.1002/cptc.202100040.
52 C. Giampietri, S. Petrungaro, M. Cordella, C. Tabolacci, L. Tomaipitinca, A. Facchiano, A. Eramo, A. Filippini, F. Facchiano and E. Ziparo, *Int. J. Mol. Sci.*, 2017, **18**, 1271.
53 The blue, green, yellow and red color channels of the microscope respectively correspond to the commonly used stains DAPI, FITC, Y3 and Y5 and are their excitation/emission windows are as follows: blue (Ex 325–375 nm, Em 435–485 nm); green (Ex 460–500 nm, Em 512–542 nm); yellow (Ex 532–558 nm, Em 570–640 nm) and red (Ex 590–650 nm, Em 662–738 nm).
54 T. Smolič, P. Tavčar, A. Horvat, U. Černe, A. Halužan Vasle, L. Tratnjek, M. E. Kreft, N. Scholz, M. Matis, T. Petan, R. Zorec and N. Vardjan, *Glia*, 2021, **69**, 1540–1562.
55 H. Liu, L. Wang, M. Lv, R. Pei, P. Li, Z. Pei, Y. Wang, W. Su and X.-Q. Xie, *J. Chem. Inf. Model.*, 2014, **54**, 1050–1060.